Spin waves in exchange spring nanoheterostructured amorphous/nanocrystalline films

Arindam Samanta [1,2] Gianluca Gubbiotti [3] and Saibal Roy [1,2,*]

[1] *Micropower Devices and Nanomagnetics Group, Tyndall National Institute, Cork, T12R5CP, Ireland*

[2] *School of Physics, University College Cork, Cork, T12YN60, Ireland*

[3] *Istituto Officina dei Materiali del CNR (CNR-IOM), c/o Dipartimento di Fisica e Geologia Universita di Perugia, I-06123 Perugia, Italy*

(Received 7 December 2021; revised 17 May 2023; accepted 2 June 2023; published 29 June 2023)

We investigate the structural, static, and dynamic magnetic properties of exchange spring (ES) nanoheterostructured, stress-free, optically smooth films of amorphous/nanocrystalline Co-rich cobalt phosphorous (CoP) prepared by electrodeposition technique at room temperature. Static magnetic measurement reveals different hysteresis loop structures of the thin films — evolution from the low coercivity non-ES loop to the staircase-ES loop, giving rise to multiple coercivities for relatively higher thickness films. The first-order reversal curve (FORC) distributions demonstrate the different reversal mechanisms present in the samples and confirm the non-ES and ES natures of the films. The field-dependent Brillouin light scattering (BLS) spectra of the ES thin film unveil two well-resolved spin wave peaks associated with the bulk modes (*B*) and the so-called Damon-Eshbach (DE) surface spin wave modes (*S*) while that for non-ES low coercivity sample show a doublet of modes below a certain value of the applied field. Observation of the *S* mode only on one side of the measured spectra depends on the direction of the external magnetic field due to the nonreciprocal character of the *S* wave in the micrometer thickness of the investigated films. The external magnetic field-dependent BLS spectra yield an almost linear dependence of the mode frequencies versus the magnetic field intensity. Studied BLS measurements demonstrate the evolution of the ES structure in 5.7-μm-thick nanohetero-structured CoP film compared to the 1.4-μm-thick non-ES sample. Additionally, the increase in the interfacial exchange energy value ($J_I^{ES} - 10.12$ erg/cm^2) in the 5.7 μm film compared to that ($J_I^{\text{non-ES}} - 3.68$ erg/cm^2) of 1.4-μm film (calculated from corresponding asymmetric peak fittings to the measured BLS spectra) reduces the interfacial exchange energy ratio ($J_I^{\text{non-ES}}/J_I^{\text{ES}}$) below unity, confirming the enhanced strength of the exchange coupling in the developed ES film.

DOI: 10.1103/PhysRevB.107.214449

I. INTRODUCTION

Conventional nanomagnetic thin films offer either high saturation magnetization with low coercivity (soft magnetic materials) or moderate saturation magnetization with a high coercivity (hard magnetic materials). However, such thin films can deliver the advantages of both types simultaneously if they are consisted of alternate (bi/tri) layers and exchange-coupled at the nanometer scale. Exchange spring (ES) [1–5] nanohetero-structured (NHS) systems, in which both the hard and soft magnetic materials are tuned (compositions, thicknesses, and morphologies) at the nanometer scale to provide a high-energy product ($BH_{\max}$) [4–6], has taken keen attention because of its potential applications in recording media [2], spintronics [7,8], spin torque nanooscillator (STNO) devices [9], and so on. The formation of the ES systems is generally favored by the critical conditions, i.e., the thickness (L_S) of the soft phase being larger than twice the domain wall width (δ_H) of the hard phase $L_S > 2\delta_H$ [5], where the soft and hard phases reverse at the distinguishable field at the same time and act like different units in the same system.

A flurry of research articles on these ES systems were published in the last three decades [1–13], and consequently, using various combinations of materials such as nanocomposites [10], bilayer thin films [14–19], magnetic trilayer structures [20] in multiple systems have been studied. Several techniques, such as magnetron sputtering [21], molecular beam epitaxy (MBE) [22], and heat treatment, including rapid annealing [23], have been utilized for developing ES NHSs. However, those ES structures were constituted with the *ex situ* process of the deposition of multinanolayer/structures and were studied mostly with static magnetic measurements [24]. Lately, ES systems have been studied through dynamic measurements [4,25–29]. However, the ES system has not been reported to date in an *in situ* single nanohetero-structured (NHS) thin film prepared through the electrodeposition technique and characterized through their dynamic measurements. Here, it is worth mentioning that the term "*ex situ*" means the bi/trilayer structures are prepared with two/multiple different sources of materials (namely, multiple targets in sputtering techniques), while the "*in situ*" term signifies that a single source of materials (in an electroplating bath) could be sufficient to prepare bi/trilayers nanohetero structures. For example, to prepare the SmCo/Fe or NiFe/[Co/Pt] ES structures, two different sputtering targets have been used. However, in this reported work, the NHSs were prepared from a single bath itself, without requiring a second bath in the electrodeposition process for generating the bilayer structures. We chose an electroplating technique to fabricate ES NHS

*saibal.roy@tyndall.ie

due to its low cost and high yield, which lends itself around complex nanotopologies [30,31]. Though thin films of cobalt phosphorous alloys (CoP) were prepared by electrodeposition technique, and were extensively studied by several groups [32–40], however, the emergence of ES magnetic structure in an *in situ* amorphous and nanocrystalline CoP film as a result of the self-organized process from a single-bath electrochemical deposition technique has not been identified/studied and reported yet.

In this work, we demonstrate the ES magnetic structure in a stress-free, optically smooth nano-hetero-structure (NHS) of a single CoP thin film developed by a modified stable acidic bath chemistry in an electrodeposition process. Consequently, by performing the measurements with a scanning electron microscope (SEM) and energy dispersive x-ray spectroscopy (EDX), x-ray diffractometer (XRD), and cross-sectional transmission electron microscope (TEM), we determined the surface morphology at the micron to the nanometer scale, composition, and the cross-sectional NHSs of the thin films. Crossover from the low coercivity non-ES system to the ES magnetic structures at room temperature has also been demonstrated using quasistatic magnetic hysteresis loop measurements and first-order reversal curve (FORC) measurements. Subsequently, we further studied the non-ES and ES structured CoP samples by Brillouin light scattering (BLS) spectroscopy and investigated the effect of interfacial exchange energy.

Contextually, it is imperative to mention that the exchange energy plays a crucial role in realizing the exchange coupled nanohetero-structured systems, irrespective of the ES or non-ES structures. Since thus-prepared *in situ* systems have significantly increased the number/volume of interfaces compared to the conventional multinanolayered systems, it is important to study the effect of the interfacial exchange coupling in the system. Brillouin light scattering (BLS) spectroscopy is a powerful technique to investigate the effect of such interfacial exchange coupling (J_I) in the NHS system.

II. EXPERIMENTAL METHODS

The following chemicals and reagents [37] are used for preparing smooth, shiny CoP thin film utilizing the electrodeposition technique at room temperature (293 K): Phosphorous acid (3.30), phosphoric acid (5.90), cobalt chloride hexahydrate (18.87), cobalt carbonate (1.55), glycine (1.15), saccharine (1.51), NTA (1.52)—the values in the parentheses are the amount of the chemicals in g/100 mL. The pH of the bath is maintained between ∼0.72–0.86.

The electrodeposition of CoP thin film using direct current (dc) plating on 2 cm × 2 cm Si-wafer with top conducting seed layer of 10 nm Ti and 200 nm Au was carried out utilizing a CHI 660B potentiostat. A constant dc of 40 mA was applied for 15 and 60 minutes. The microstructural analysis and elemental characterization of the electrodeposited films were performed using the Zeiss Scanning Electron Microscope (SEM) and Energy Dispersive X-ray Spectroscopy (EDX) analysis (Oxford Instruments). The TEM lamella cross-sections were prepared using a Dual Beam focused ion beam (FIB) of FEI Helios NanoLab 600i. To protect from the FIB milling process, three layers of C/Pt/Pt were deposited on the sample within the Dual Beam FIB (50 nm/300 nm by the electron-beam-induced deposition/ 2 μm by ion-beam-induced deposition). The lamella was prepared and thinned down for the TEM analysis. The thinning at 30 kV was finished with a final polishing at 5 kV (47 pA) to reduce the ion-beam-induced damage to less than 2-nm thin layers on both sides. Ultrafine microstructural analysis was performed through TEM (Jeol 2100; 200 kV) using a double tilt sample holder. The x-ray diffraction (XRD) patterns were measured through the Panalytical X'Pert Pro setup with Cu K_α radiation (40 kV, 50 mA) at a wavelength of 0.154 nm to characterize the crystalline/amorphous structures.

The magnetic measurements of the deposited films were carried out in a hysteresis Loop tracer (MESA 200, ShB Instruments, USA). The FORC measurements are done with Quantum Design Physical Property Measurement System (PPMS) Versalab (USA) with VSM-FORC option. The PPMS system was used to measure a large number [229 for Sample 1 (here after as the non-ES sample) and 159 for Sample 2 (here after as the ES sample)] of FORCs. Typical FORC measurements are done as follows. First, the sample is saturated and then the moment was measured starting from a reversal field H_R back to positive saturation ($+H_{\text{sat}}$), that traces out a FORC. A family of FORCs was yielded for different values of H_R, with equal field spacing (H_F). Following that, the FORC distribution is extracted by a mixed second-order derivative $\rho(H_R, H_F) = -\frac{1}{2M_S}\left(\frac{\partial^2 M(H_R,H_F)}{\partial H_R \partial H_F}\right)$, where M_S is the saturation magnetization. The FORC measurement ensures that the purely reversible components of the magnetization are eliminated, and thus any nonzero ρ corresponds to irreversible switching processes present in the system [41–43]. Here, the FORC distribution $[\rho(H_C, H_U)]$ is presented on the (H_C, H_U) plane, defining, $H_C = \frac{1}{2}(H_R - H_F)$ as the local coercivity, and $H_U = \frac{1}{2}(H_R + H_F)$ as the interaction field or bias field obtained by postprocessing the raw data with FORCINEL Software [44].

The Brillouin light scattering (BLS) spectroscopy [27–29] was used to measure the thermally excited SWs in the frequency range between 1 and 50 GHz. The BLS measurement was operated using a single-mode diode-pumped solid state laser at wavelength, $\lambda = 532$ nm monochromatic laser light with an incidence angle of ∼10 degrees with respect to the sample normal, which results in a magnon wave number, $k_{||} = 2k_i \sin\theta = 4.1 \times 10^6$ rad/m, ($k_i = 2\pi/\lambda$). The backscattered light has been analyzed utilizing a Six $(3+3)-$ pass Sandercock-type tandem Fabry-Perot interferometer. An external magnetic field (H) was applied parallel to the film surface and perpendicular to the plane of incidence of the light, i.e., the Damon-Eshbach configuration.

III. RESULTS AND DISCUSSION

A. Structural characterization and elemental analysis

The initial instability of the electrolytic bath causes the development of quite stressed and rough thin films, even for the comparatively lower thicknesses (∼0.50 μm) of the film, as shown in Fig. 1(a). The possibility of such high stress

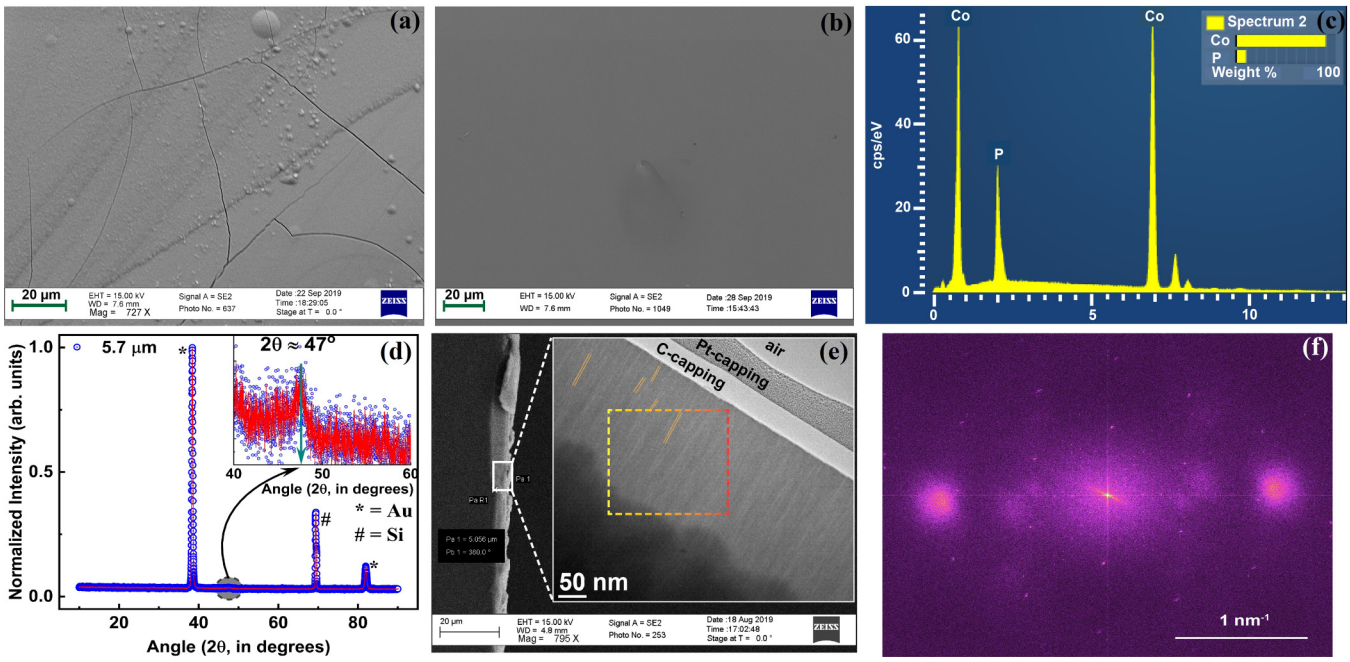

FIG. 1. Typical SEM top surface morphology of the (a) stressed thin film, (b) stress free thin film, (c) EDX spectrum of one of the samples, (d) XRD-spectrum of the sample, (e) cross-sectional TEM micrograph of the electrodeposited CoP thin films showing the individual striations (white lines in the NHS) in (thickness 2 to 5 nm) nm range, typical, and (f) FFT of the selected region of TEM as highlighted in (e).

might be due to presence of high surface tension between the working electrode and the electrolyte, which causes the samples to be stressed with microcracks, rough, and thus incompatible for the BLS measurements. A surface-tension-reducing agent—glycine, stress-relieving additives—a combination of naphthalene trisulfonic acid (NTA) and saccharine [45,46] were added to the solution to stabilize the bath and to reduce the surface tension between the working electrode and electrolyte. Consequently, stress-free, smooth, and glossy thin films were developed even for the comparatively higher thicknesses (∼1.4–5.7 μm) of the film. Figure 1(b) shows a typical stress-free film of 1.4-μm thickness. The top surface quality of the film remains unaltered even for the 5.7-μm-thick film.

Since the phosphorous content in the CoP thin film plays a crucial role in determining the crystallinity of the CoP thin film, it is important to explore the qualitative and quantitative analysis of phosphorous in the electrodeposited thin film [47]. A typical example of the EDX spectra of the CoP thin film (here, for the 1.4 μm film) is shown in Fig. 1(c), confirming the different dominant Co and P peaks. For example, the peaks at 0.77 keV, 6.93 keV, and 7.64 keV unveil the L_α, $K_{\alpha 1,2}$, and K_β peaks of "Co," while the peak at 2.13 keV corresponds to the K_β peak of "P," respectively. EDX study at different places of the film yields the similar stoichiometry of the thin films, i.e., the overall atomic percentage of cobalt (86%) and phosphorous (14%) in the CoP thin films remains almost invariant, which corroborates the homogeneity in the composition of the films. We also observed that the deposited films retain their stoichiometry for a long deposition time. We obtained this improvement due to the addition of the stabilizing agent in the plating bath, which restrains the bath from precipitating over a long period.

Figure 1(d) shows the XRD pattern of the prepared 5.7 μm nanohetero-structured CoP thin film with the three dominating substrate peaks only, i.e., the peak near $2\theta = 69.22^\circ$ (Si-wafer) and the other two peaks near $2\theta = 38^\circ$ and 83° (top conducting Au-seed layer), hence the gross amorphousness of the prepared samples has been verified. However, the magnified XRD profile [inset in Fig. 1(d)] shows a minor and broad peak at $2\theta \sim 47^\circ$, which confirms that the samples also have a nanocrystalline Co-hcp (002) phase. Though, the overall XRD spectra with three dominant substrate peaks do not exhibit a significant difference, however, there is a subtle change observed in the magnified XRD spectra in terms of minor peaks, resulting in a subtle change in the nanocrystalline structure due to the increase in the film thickness. For the 1.4-μm-thick film (not shown in the main paper), there were two minor peaks at $2\theta \approx 45^\circ$ and $2\theta = 77.5^\circ$, which signify the coexistence of nanocrystalline Co-hcp (002) and Co-hcp (110) phases, respectively.

Nanohetero-structures/multinano-layers in the ES CoP system were experimentally confirmed by the cross-sectional TEM as shown in Fig. 1(e). Here, the white lines in the TEM image correspond to the Co-hcp phases and the black regions correspond to amorphous CoP, where the individual striped nanocrystallites with 2 to 5 nm thicknesses (Co-hcp phases), as measured from the TEM, are embedded within the amorphous matrix (CoP phase). The fast Fourier transformation (FFT) of the selected region of the TEM image in Fig. 1(e) is shown in Fig. 1(f) confirms the crystalline nature of the film which could be attributed to the nanocrystalline phases present in the sample.

However, from XRD [as shown in Fig. 1(d)], for the 5.7-μm film, the relative intensity of Co-hcp (002) phases is increased compared to the 1.4 μm-film. Hydrogen evolution

during electrodeposition might have favored the formation of these hcp textures. The size of the crystalline phase in the nanohetero-structured film as calculated utilizing the Scherrer equation [$\tau = \frac{\kappa \cdot \Lambda}{\beta \cos\theta}$, where τ is the mean grain size, κ is a dimensionless shape factor with a value close to unity, Λ is the x-ray wavelength (1.54 Å), β is the line broadening at the full width at half the maximum intensity (FWHM) of the crystalline peak, and θ is the Bragg angle (in degrees)] is found to be $\approx (1.239 \pm 0.143)$ nm, which is in the same order of the Co-hcp stripe thickness obtained from the TEM. Therefore, while the surface morphology remains unaltered with the increase in overall thickness, a subtle nanocrystalline structural variation with enhanced out-of-plane (OOP) anisotropy (as further detailed below) is observed.

To investigate the nature of the anisotropies present, we need to study the constituent energies of the system. The total energy (1) can be written as an integral over the sample volume [48]

$$E_{\text{total}} = \int [w_{ex} + w_a + w_d + w_z + w_{me}]dV, \qquad (1)$$

where "w" denotes the corresponding energy density of the material. The symmetric exchange energy density is $w_{\text{ex}} = A_{\text{ex}}\nabla(\vec{m})^2 = A_{\text{ex}}[\nabla(\vec{m}_x)^2 + \nabla(\vec{m}_y)^2 + \nabla(\vec{m}_z)^2]$ (A_{ex} being the exchange stiffness constant). "w_a" is the anisotropy energy density (due to the crystallinity of the material). The stray-field energy density or magnetostatic energy density is $w_d = \int (\frac{1}{2}\mu_0 \vec{H}_d \cdot \vec{M})dV$. "$w_z$" is the external energy density or Zeeman energy density $= \mu_0 \vec{H} \cdot \vec{M}$, and the last term, '$w'_{me}$ is the magnetoelastic (ME) energy density $= k.\lambda_s \cdot \sigma_p \cdot (S)^2$, where, k = constant $(+ve)$, λ_s = magnetostriction constant, σ_p = the interfacial planar stress and "S" is the squareness ratio $= M_R/M_S(+\text{ve})$, here, M_R and M_S are the remanent magnetization and saturation magnetization of the material, respectively.

To elucidate the origin of out-of-plane (OOP) anisotropy in the system first, we consider the magnetoelastic (ME) energy density. A significant aspect of ME energy density is that, if λ_s and σ_p have opposite signs in the expression of the ME, i.e., $w_{me} = k.\lambda_s \cdot \sigma_p \cdot (S)^2$ the ME energy becomes negative (-ve) and that -ve ME energy density has the ability to produce an out-of-plane (OOP) anisotropy in the system [48]. In our ES system, the nanocrystalline Co-hcp phases are embedded in the amorphous CoP matrix. As shown in Fig. 1(e), the inset in the TEM image shows that the thickness of Co-hcp is around 2 to 5 nm. For Co-hcp, a positive value of λ_s $[(+2.50 \pm 0.20) \times 10^{-5}]$ [49] is expected above 2-nm thickness [49,50]. Earlier, experimentally, it was shown that CoP films (∼10 μm) have a $-ve$ λ_s value $[(-2.75 \pm 0.20) \times 10^{-6}]$ [51]. Hence, two different magnetostrictive material coexist in the nanohetero-structured system, which might be responsible for the generation of the compressive stress in the system, i.e., $\sigma_P = -ve$. So, the ME becomes $-ve$ and thus helps generate the out-of-plane anisotropy in the system. Therefore, it is assumed that the nanocrystalline Co-hcp (002) phases in the NHSs are responsible for the OOP anisotropies in the system, which get enhanced beyond 2-nm thickness with the simultaneous decrease in the content of nanocrystalline Co-hcp (110) phases.

B. Static magnetic properties

Experimentally obtained normalized hysteresis loops along the direction X (dir.1) and direction Y (dir.2) of the *in situ* NHS CoP materials (measured by SHB instruments) are shown in Fig. 2; dir.1 and dir.2 represent the longitudinal and transverse directions, respectively. Hence, the X and Y directions are two mutually perpendicular directions on the sample plane, i.e., both the axes, dir.1 and dir.2 (dir.2 = dir.1 + 90^o), lie in-plane to the sample. The interesting fact for all the normalized hysteresis loops is that both dir. X and dir. Y are practically equivalent, i.e., all the samples are magnetically isotropic in the XY plane and there is no identifiable easy or hard axis lying on the plane of the material. Previously, Ausanio *et al.* [50] showed that the magnetization with OOP anisotropy was inclined at an angle with respect to the sample plane in the case of isotropic hysteresis loops in the X and Y directions on the sample plane. Additionally, following the nature of the hysteresis loop as detailed below, we assume that there must be a weak OOP anisotropy present in the thinner non-ES sample.

Figure 2(a) shows a (1.4-μm film) low coercivity (∼31 Oe) non-ES hysteresis loop, while that of Fig. 2(b) (5.7-μm film) exhibits a high coercivity (∼220 Oe) ES nature with steps in the hysteresis loops along with the low coercivities (∼9 Oe and ∼31 Oe). Three distinct regions are prominent in the non-ES sample, i.e., (i) hysteresis at the applied field below ∼25 Oe, (ii) a linear region at the applied field between 25 Oe to ∼150 Oe, where the magnetization changes almost linearly with the applied field, (iii) the saturation magnetization beyond ∼150 Oe, whereas the region (ii), is a common signature of thin films having a weak perpendicular anisotropy [52]. Here, in the 1.4-μm-thick sample, in-plane (IP) anisotropy arising out of the CoP amorphous phase strongly dominates over the weak perpendicular anisotropy arising out of the Co-hcp phase.

On the other hand, a staircase-like hysteresis loop, one of the signatures of ES structure, is obtained with two distinguishable coercivities in a single material (5.7 μm), as shown in Fig. 2(b). In this case, the two different phases, Co-hcp phase (corresponds to the relatively higher coercivity) and the amorphous CoP phase (corresponds to lower coercivity), are nonrigidly coupled to each other and act as separate units in the same material. Hence, with the application of an external magnetic field, both the phases reverse at the different magnetic fields, as neither IP nor OOP anisotropy dominates each other, i.e., the OOP anisotropy becomes comparable to the IP anisotropy in the ES system, however, the sample magnetization still lies in the plane of the material even if there is OOP anisotropies present in the system. As a result, a high "S" (M_R/M_S) value (0.8333) is obtained for the 5.7-μm film, as shown in Fig. 2(b) in comparison to the "S" value (0.6234) of the 1.4-μm film as shown in Fig. 2(a).

The presence of different coercivities in 1.4 μm and 5.7 μm films is prominently visible in the corresponding differentials of the magnetization values [dir-2 (typical)] as in Figs. 2(c) and 2(d), respectively. It is interesting to note that the 1.4 μm film also has a smaller coercivity of ∼9 Oe along with ∼31 Oe, which is invisible as such in the normal hysteresis loop in Fig. 2(a). This arises possibly due

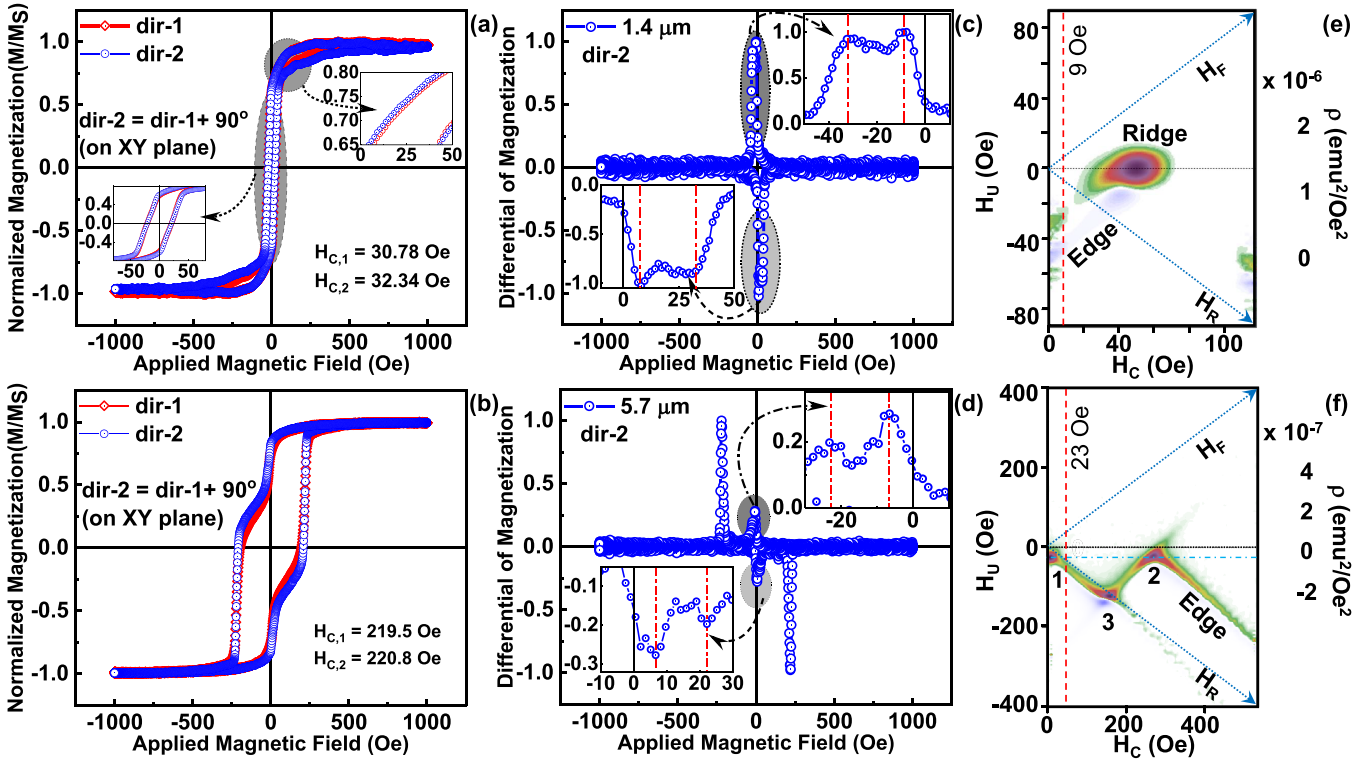

FIG. 2. Hysteresis loop of the dc electrodeposited CoP thin films measured in ShB Hysteresis Loop tracer in XY plane; here, dir-2 = dir-1+ 90°. The thickness of the films is (a) 1.4 μm, (b) 5.7 μm, for the electrodeposition time (a) 15 min, (b) 60 min, respectively. (c), (d) Differential of the magnetization of the (a) 1.4 μm, (b) 5.7-μm-thick thin films, respectively. Red dotted lines indicate different coercivities in the low field range. (e), (f) The FORC distributions on (H_C, H_U) plane for non-ES and ES samples, respectively.

to the nanohetero-structure, i.e., the presence of the Co-hcp phase within the amorphous matrix, as shown in the insets of Fig. 2(c). Similar characteristics, i.e., low coercivities of ∼9 Oe and ∼23 Oe and a comparatively higher coercivity of ∼242 Oe, are also observed for the 5.7 μm film, as shown in the insets of Fig. 2(d).

C. First-order reversal curve distribution

To comprehend the magnetic phase interactions in the nanoscale regime, we further analyzed it using minor hysteresis loop analysis, namely, FORC measurements. The corresponding FORC distributions obtained with a smoothing factor of 4 for 1.4 μm and 5.7 μm films on the (H_C, H_U) plane are portrayed in Figs. 2(e) and 2(f), respectively, displaying two completely different reversal mechanisms present in the systems. The prominent feature of FORC distribution of the 1.4 μm film is centered at $H_U = 0$ Oe and $H_C \sim 45$ Oe [Fig. 2(e)], while the ∼9 Oe peak [as observed in Fig. 2(c)] is invisible for the 1.4 μm film. Again, the FORC distribution ensures the elimination of the pure reversible components of the magnetization. Hence, the peak at ∼9 Oe in the 1.4 μm film must be the reversal phase of the system.

Figure 2(f) reveals a significant change for the 5.7 μm film, i.e., now the center has shifted to −25 Oe along the H_U axis at $H_C \sim 9$ Oe (peak 1). It is interesting to note that the ∼23 Oe peak [as observed in Fig. 2(d)] is invisible in this case. Hence, the peak at ∼9 Oe in the 5.7 μm film must be the irreversible phase present in the systems while that at ∼23 Oe confirms its reversible nature. The loop reaches the trough at $H_U \sim 135$ Oe and $H_C \sim 160$ Oe (peak 3), following that the next center arises again at $H_U = -25$ Oe and $H_C = 270$ Oe (peak 2), which necessarily means that a prominent different irreversible phase was introduced into the system along with the reversible phase (∼23 Oe). The shift in the FORC distribution on the H_C plane confirms the increment of the coercivity in the ES sample compared to the non-ES sample.

Additionally, the positive and negative signatures (edges) reveal the deviation of the hysteresis loop from an ideal hysteron. On the other hand, the complex FORC behavior of the ES sample confirms that the phases interact strongly between themselves in the nanoscale and are not independent as they are in the non-ES sample, which are imperceptible from the conventional hysteresis loop. In an ES system, the soft phase should be fully reversible [5] and the hard phase should be irreversible [3] while they are only coupled via the exchange interaction [3–5]. Though both reversible (∼9 Oe) and irreversible (∼45 Oe) phases present in the 1.4 μm film, however, lack of any exchange interaction between those phases, as is evident from the absence of any interaction peak in Fig. 2(e), make the sample non-ES system. On the contrary, the reversible ∼23 Oe and the irreversible ∼270 Oe phases are connected through a strong exchange interaction in the 5.7 μm film, as observed in Fig. 2(f) (peak 3 of ∼160 Oe) and make the 5.7 μm film as an ES system. The tiny shift (−25 Oe) in the H_U value is due to the exchange interaction present in the ES system [41,42] and this small amount of field might be due to the ES effect, as explained earlier.

In the FORC study, the magnetic field is first saturated and then reduced from that positive saturation to small negative fields, where the high coercivity phase (possibly Co-hcp, here) remains positively saturated while the low coercivity phase follows the field reversibly, which then relaxes to a positive orientation in the absence of a field due to the exchange coupling to the high coercivity phase. In the following sections, we elucidate it analytically.

D. Analytical formulation

We consider here the influence of NHS in the exchange energy. If the next-nearest-neighbor exchange constant J_2 is considered along with the term J_1, the number of atoms having IP anisotropy is denoted as N_1 while that of OOP anisotropy is N_2; $A^1_{\rm ex}$ and $A^2_{\rm ex}$ being the exchange stiffness constant of the IP and OOP anisotropy parts, respectively, so the energy value becomes (see the Supplemental Material [66] for a detailed calculation)

$$E_{\rm ex} = N_1 A^1_{\rm ex} \int_V I_1 d^3r + N_2 A^2_{\rm ex} \int_V I_2 d^3r. \tag{2}$$

Considering the non-ES and ES systems in the studied samples, we can comparatively say that the exchange energy present in the ES system ($E^{\rm ES}_{\rm ex}$) is greater than that in the non-ES system ($E^{\text{non-ES}}_{\rm ex}$), as $N^{\rm ES}_2$ is greater than $N^{\text{non-ES}}_2$ due to the increase in the thicknesses of the individual striations of the grown NHS, i.e.,

$$\frac{E^{\rm ES}_{\rm ex}}{E^{\text{non-ES}}_{\rm ex}} = \frac{N^{\rm ES}_1 A^1_{\rm ex} \int_V I_1 d^3r + N^{\rm ES}_2 A^2_{\rm ex} \int_V I_2 d^3r}{N^{\text{non-ES}}_1 A^1_{\rm ex} \int_V I_1 d^3r + N^{\text{non-ES}}_2 A^2_{\rm ex} \int_V I_2 d^3r} \tag{3}$$

$$\Rightarrow \frac{E^{\rm ES}_{\rm ex}}{E^{\text{non-ES}}_{\rm ex}} > 1 \qquad [as, \quad N^{\rm ES}_2 > N^{\text{non-ES}}_2]. \tag{4}$$

As the $E_{\rm ex}$ term is independent of any overall thickness parameter, it could be mentioned that the evolution of ES is not directly related to the overall thickness of the film; rather, it depends on the thicknesses of the individual striations of the internal nanohetero-structures grown inside the film. This enhanced exchange energy in the thicker samples being the exchange between relatively stronger OOP anisotropies of Co-hcp nanostriations and IP anisotropy of the CoP amorphous matrix help create an ES state with higher coercivity and signature step-hysteresis loop.

E. Brillouin light scattering spectroscopy

We further study thermally excited magnons using Brillouin light scattering (BLS) spectroscopy for understanding our ES nanohetero-structured system, as BLS spectroscopy allows to measure the frequency of the thermally excited spin waves in the absence of any external stimuli such as the microwave driving magnetic field, electric field, electrical current, or optical pumping [53,54] compared to available techniques for dynamic measurements, e.g., the vector-network analyzer ferromagnetic resonance (VNA-FMR) measurement [2,55] or time-resolved magneto-optic Kerr (TRMOKE) effect [2,56,57].

During a typical BLS measurement, a focused laser beam interacts with the sample and the photons are inelastically scattered by the spin waves [58]. Momentum and energy conservation causes the annihilation of magnons (anti-Stokes process) and the creation of magnons (Stokes process). The linewidth of the inelastic peaks (i.e., the BLS spectra) relates to the magnetic inhomogeneity [59], while that of the elastic peak reveals the instrumental linewidth broadening [60]. Here, the BLS measurements are performed by saturating the sample in a 1.5-kOe magnetic field and reducing it down to 0.25 kOe, thus following the descending branch of the hysteresis loop as shown in Fig. 2. In this field range, the magnetization is always saturated and parallel to the applied magnetic field. As the thickness of the striations of NHSs increases in the ES system compared to that of the non-ES sample, the laser light interacts more with the available spins in the ES system compared to the non-ES sample. This might be the reason behind the appearance of the pronounced surface spin wave in the ES system. Sequences of BLS spectra measured at different H values are shown in Figs. 3(a) and 3(b) for the 1.4-μm- and 5.7-μm-thick films, respectively.

Spectra for the 1.4 μm films show almost similar characteristics (only one broad peak B, as mentioned in the figure) on both the sides of the spectra, whereas the 5.7 μm film consists of two well-resolved distinct peaks (S and B, as mentioned in the figure) on the Stokes side of the spectra. Here, B stands for a band of bulk modes at the low frequency and S for the surface spin wave corresponds to the higher frequency (sharp peak), the so-called Damon-Eshbach (DE) surface spin wave [61]; which propagates in the film plane. The S mode is observed only on one side of the spectrum depending on the direction of the external magnetic field,which is the consequence of its nonreciprocal character within the micrometer thickness of the investigated films. A careful observation of the BLS spectra of the 1.4 μm film reveals that the peak shape on the Stokes side of the spectra is broadened compared to that of the anti-Stokes side for an applied bias field larger than 1 kOe. However, below 1 kOe, the DE/S mode is shouldered to the B mode and a wide peak on the Stokes side has appeared due to the small frequency difference between the DE/S and B mode. This double peak structure could be ascribed to the hybridization between B and DE/S mode, as previously observed by Sandercock [61]. The S mode in the 5.7 μm film is observed only on one side of the spectrum depending on the direction of the external magnetic field, which is the consequence of its nonreciprocal character within the micrometer thickness of the investigated films [61]. The BLS spectra, as shown in Fig. 3(c), reveal the effect of magnetic field reversal at constant magnitude of 1.0 kOe, which unveils the predicted side change of DE surface mode due to its nonreciprocal spatial localization.

Additionally, we study the external magnetic field-dependent BLS spectra for both the samples, which show an almost linear dependence of the mode frequencies vs the magnetic field intensity, as shown in Fig. 4. A careful observation reveals the dissimilarity in the bulk mode frequencies of 1.4-μm- and 5.7-μm-thick samples, respectively. Figure 4(a) unveils that the bulk mode frequencies follow the typical Kittel curve (red curve in the figure) with the least deviation, however, below 9.26 GHz frequency in Fig. 4(b), that deviate from the typical Kittel curve, with a downward shift in frequency (where γ = gyromagnetic ratio, H = magnetic field, M_S = saturation magnetization). To fit the experimentally

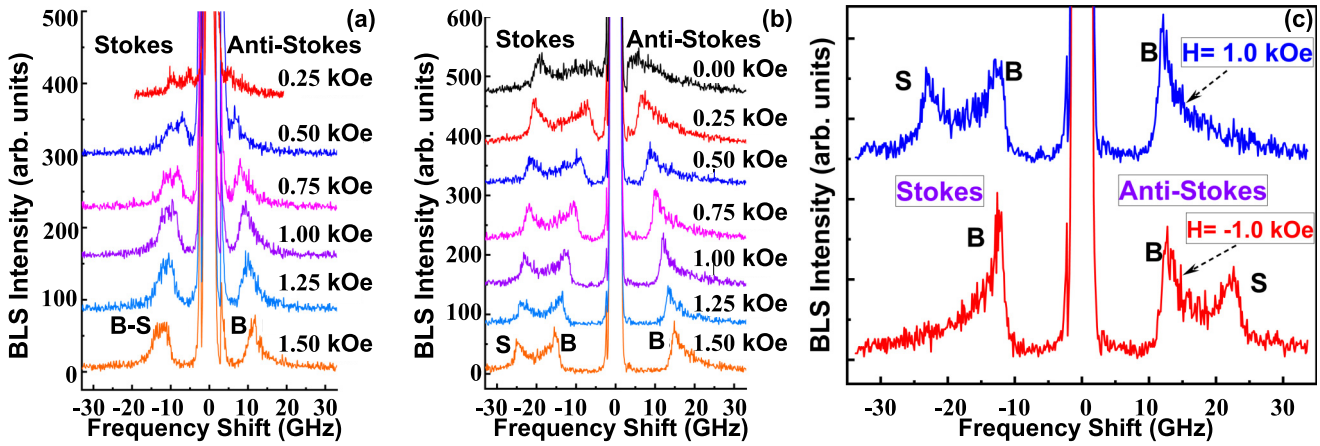

FIG. 3. BLS Spectra of (a) non-ES (1.4 μm) and (b) ES (5.7 μm) CoP thin film at different in-plane bias magnetic fields measured from (a) 1.50 kOe to 0.25 kOe and (b) 0.00 kOe with the backscattering geometry. (c) BLS Spectra of 5.7 μm in a bias magnetic field of +1.0 and −1.0 kOe revealing the effect of the reversal of the magnetization on the frequency position of the Damon-Eshbach wave.

obtained bulk magnon frequencies, the typical Kittel formula is modified by adding the exchange field, H_U to the applied bias field H, which results in H_{eff}, i.e., $H_{\text{eff}} = H + H_U$. The experimental data are well fitted with the modified Kittel curve (5) [61] (blue curve in the figure)

$$\omega_B = \gamma\sqrt{H_{\text{eff}} \cdot (H_{\text{eff}} + 4\pi M_S)}. \tag{5}$$

It is noted that in the low field regime (<200 Oe), we could not measure the spectra properly. So, in the subsequent paragraph, we report the H_U value from the DE mode, as shown in Fig. 4(c), following a similar approach by Haldar *et al.* [27]. Further, we analyze the field evolution of the surface Damon-Eshbach mode, as shown in Fig. 4(c), by using the analytical formula [Eq. (6)] valid for a semi-infinite medium [61]. The fitted line shows almost linear frequency dependency of the DE mode with respect to the applied magnetic field

$$\omega_{\text{DE}} = \gamma \cdot (H_{\text{eff}} + 2\pi M_S). \tag{6}$$

As observed from the FORC measurement [Fig. 2(f)], a weak exchange coupling should exist between the multi-nanolayers of the nanohetero-structure of the *in situ* ES CoP thin film. Therefore, considering the exchange field $H_U = -25.30$ Oe as input in the equation, the fitting yields gyromagnetic ratio $\gamma = 30.02 \times 10^{-4}$ GHz/G and saturation magnetization, $4\pi M_S = (13188 \pm 56)$ G [(12233 ± 376) G from bulk peak fitting]. There is a little misfit between the saturation magnetization ($4\pi M_S$) values obtained from the bulk and surface peak fitting results, possibly due to the weak out-of-plane anisotropy present in the system or might be due to the thick sample and experimental limitation with the dynamic study. In BLS measurements, usually, the outermost layer (∼15–20 nm) of the samples can be probed while the quasistatic magnetic measurements probe the entire sample volume, thus providing information on the overall sample magnetic parameters [62]. Moreover, the gyromagnetic ratio (γ) is related to the magnetomechanical ratio (g) through, $\gamma = g(\frac{\mu_B}{\hbar})$, where μ_B is the Bohr magneton and $\hbar$ is the reduced Planck's constant. So $\gamma = 30.02 \times 10^{-4}$ GHz/G yields $g = 2.15$. Such slightly larger g values (i.e., $g > 2$) were observed before [27] and could possibly be due to complex nanohetero-structures.

It is worth mentioning that the sharp and almost symmetric shape of the surface peak detected in the BLS spectra is due to the fact that for metallic (opaque) material the in-plane component of the wave vector is conserved in the scattering process and therefore fitting the surface peak by a Lorentzian (symmetric) curve is a valid assumption. On the other hand, the asymmetry in the shape of the bulk peak of the

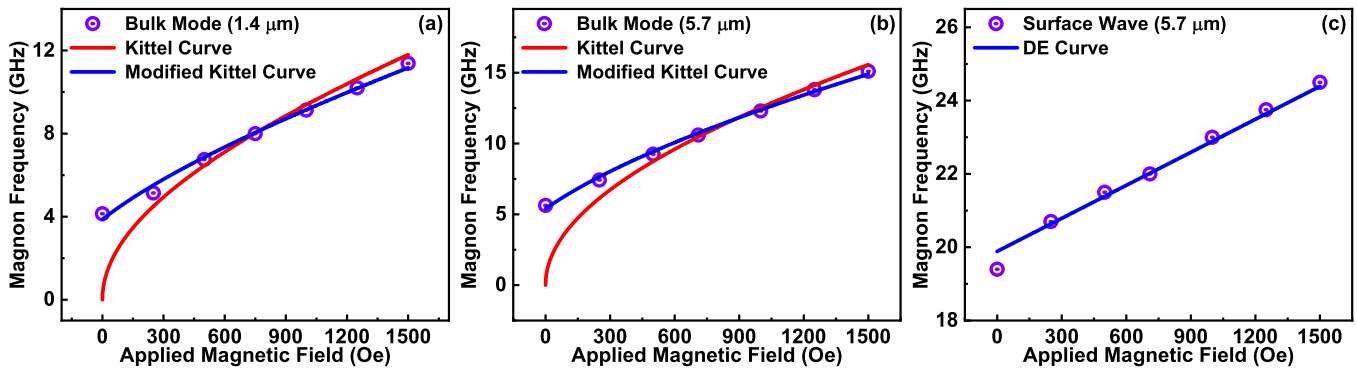

FIG. 4. Spin-wave frequencies of (a) bulk mode (1.4 μm non-ES film), (b) bulk mode of ES, and (c) Damon-Eshbach surface wave as a function of magnetic field of 5.7 μm ES CoP thin film.

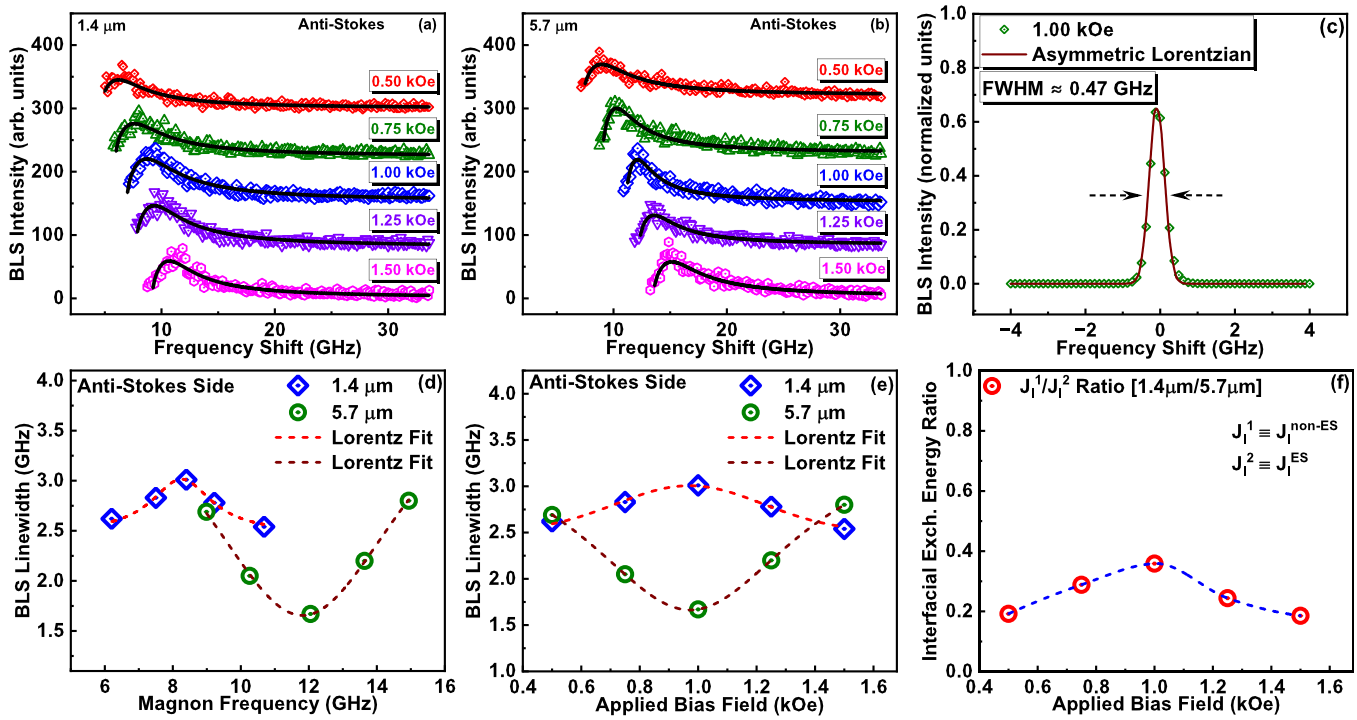

FIG. 5. Lorentzian fittings of the anti-Stokes BLS peak as a function of magnetic field of (a) 1.4 μm non-ES and (b) 5.7 μm ES CoP thin film. (c) Lorentzian fitting to a typical elastic peak in the BLS spectra. BLS linewidth (Δf) as a function of (d) corresponding anti-Stokes magnon frequencies and (e) applied bias magnetic field for 1.4 μm and 5.7 μm thick thin films. (f) The J_I^1/J_I^2 ratio as function of bias magnetic field. The symbols correspond to the experimental data while the lines joining the symbols are guide to eyes.

investigated CoP films is due to the concomitant effect of several factors.

For thick ferromagnetic films, the bulk mode (perpendicular standing spin waves, PSSW) have the perpendicular component of the wave vector ($k_\perp$) that is quantized according to the simple expression $k_\perp = n\frac{\pi}{d}$, where d is the film thickness and n is an integer number. These modes have a stationary character with an oscillatory profile across the film thickness with a BLS intensity reduction, on increasing the mode number n [63]. Furthermore, on increasing d, these modes condensate toward the frequency value of the lowest order PSSW mode forming a continuous band of modes with the high density of magnonic states there.

An additional effect is that, due to the finite penetration of light into an opaque material, in the direction perpendicular to the surface the laser light sees only a limited extent of the excitation with the result that from the uncertainty principle, the wave-vector component, $k_\perp$ is not conserved. This spread is responsible for the fact that several PSSW modes enter into the scattering process [61] giving rise to the broad and asymmetric lineshape peaking at the low frequency.

Considering all these effects, we use the theory from Cottam [64] for fitting the asymmetric peak lineshape associated to the bulk mode with light scattering from spin-waves in absorptive (opaque) magnetic materials. This theory introduced the concept of the "opacity broadening" contribution to the peak linewidth associated to a complex refractive index of the material.

The obtained BLS linewidths (Δf) of the corresponding bulk magnon frequency (f) peaks on the anti-Stokes side for 1.4 μm non-ES and 5.7 μm ES films, as shown in Fig. 5(a) and 5(b) are utilized to calculate the ratio of the interfacial exchange energy [J_I in Eq. (7)] for two different systems (i.e., ES and non-ES) [27]. An estimate of instrumental linewidth broadening, as shown in Fig. 5(c), is obtained with the Lorentzian fitting to a 1.00-kOe elastic peak of the BLS spectra of 1.4 μm film [59,60]. The fitting procedure yields the value of linewidth broadening of 0.47 GHz, which provides the lower limit of the linewidth measurement in our BLS spectra and is uniformly present in the BLS signal for all the measurements. The anti-Stokes linewidths (Δf) as a function of magnon frequency, as shown in Fig. 5(d) for 1.4 μm film, reached the peak in the beginning and decreased gradually, while that of 5.7 μm film first hit a trough and then increased again. A similar behavior in linewidth variation as a function of applied bias magnetic field is observed, as shown in Fig. 5(e). The reduction in the initial linewidth value obtained in the ES system compared to the non-ES system indicates a significant variation in the damping parameter with the evolution of ES spring morphology. Moreover, it is assumed that the interfacial exchange energy gradually becomes comparable with the exchange energy within the layer [4], resulting in a trough in the linewidth variation with the applied bias field in case of the ES sample; subsequently, the linewidth increases again while the interfacial exchange dominates over the exchange within the layer

$$\Delta f = \frac{\gamma^2 \langle A_d \rangle p \langle \cos^2 \alpha \rangle \zeta}{A_{\text{ex}} \cdot f} \left(\frac{J_I}{t}\right)^2. \tag{7}$$

Since the data are not deconvoluted, the linewidth variation presented here, as shown in Figs. 5(d) and 5(e), includes the contribution coming from instrumental broadening [60]

and from the intrinsic spin-wave damping (Gilbert damping). The sharp decrease in linewidth with increasing frequency for the non-ES film indicates extrinsic contribution (interfacial roughness or structural inhomogeneity) to the magnetic inhomogeneity in this film [59].

Here, γ is the gyromagnetic ratio, $\langle A_d \rangle$ is the surface area, p is the fraction of defects, α is the angle between the moments of two consecutive layers, ζ is a numerical factor, A_{ex} is the exchange stiffness constant $= \frac{1}{2} \cdot D \cdot M_S$, J_I is the interfacial exchange energy, and t is the probed thickness in the BLS measurements. From the BLS spectra of 1.5-kOe-applied bias magnetic field data, Eq. (7) yields the J_I values approximately as 3.68 erg/cm^2 and 10.12 erg/cm^2 for 1.4 μm and 5.7 μm films, respectively, with an assumption $\langle \cos^2 \alpha \rangle = 0.5$ and the numerical factor ζ as 0.55 [27,65]. The interfacial exchange energy ratio as a function of the applied bias magnetic field is shown in Fig. 5(f). Increments in the J_I value for 5.7 μm film with respect to that of 1.4 μm film reduce the interfacial exchange energy ratio, i.e., $J_I^{\text{non-ES}}/J_I^{\text{ES}}$ below unity (as $J_I^{\text{ES}} > J_I^{\text{non-ES}}$), which confirms that the strength of the exchange coupling in ES is greater than the non-ES film.

IV. CONCLUSION

In summary, we fabricated optically smooth, nanohetero-structured, amorphous-nanocrystalline CoP thin films using the electrodeposition technique at room temperature and demonstrated the evolution of the ES state from the *in situ* non-ES state within such films starting in a single alloy material. The existence of the NHS in the system is confirmed by XRD, TEM, and FFT of TEM. The static magnetic properties of nanohetero-structured CoP thin films characterized by magnetic hysteresis loop measurements show a signature of the ES nature in the system and were further corroborated by FORC measurements. The existence of *in situ* ES systems was supplemented by dynamic characterization using BLS. Only bulk mode on both the Stokes and anti-Stokes sides of the relatively thinner film has appeared, and an additional peak appears, as a shoulder of the B mode, on the Stokes side of the spectra, which could probably be ascribed to the S mode that is hybridized with the B mode. On the other hand, in the relatively thicker system, well-resolved distinct bulk and surface modes on the Stokes side and only bulk mode on the anti-Stokes side have appeared. The increment in the coercivity and interfacial exchange energy value in the 5.7 μm film compared to the 1.4 μm film confirms the presence of increased exchange interaction in 5.7 μm film compared to that in the 1.4 μm film. Our study offers an approach to preparing the ES structure in a cost-effective and scalable manner, opening the door to modifying the magnetic properties even in a single ferromagnetic thin film. Thus, it provides a novel pathway to use these materials and their derivatives as next-generation recording media and potentially for the next-generation optically induced spin transfer torque (STT) devices.

ACKNOWLEDGMENTS

A.S. and S.R. thank the Science Foundation Ireland (SFI) Frontiers for the Future Programme (FFP) Award Grant (Grant No. SFI-21/FFP-A/10003-MERIT) for funding this work. Research at IOM-CNR was funded by the European Union-Next Generation EU under the Italian Ministry of University and Research (MUR) National Innovation Ecosystem Grant No. ECS00000041 - VITALITY. G.G. acknowledges Universitá degli Studi di Perugia, CNR, and MUR for support within the project VITALITY. G.G. also acknowledges support from the Italian Ministry of University and Research through the PRIN-2020 project entitled "The Italian factory of micromagnetic modeling and spintronics", code: 2020LW-PKH7. The authors thank R. K. Dumas of Quantum Design, USA for performing the FORC measurements (done at the Quantum Design Application Laboratory, USA). The authors thank B. Sheehan of Tyndall National Institute for preparing the FIB samples and TEM measurement. The authors also thank M. G. Cottam of the Department of Physics and Astronomy, The University of Western Ontario for fruitful discussion.

[1] E. F. Kneller and R. Hawig, The exchange-spring magnet: A new material principle for permanent magnets, IEEE Trans. Magn. **27**, 3588 (1991).

[2] M. Dąbrowski, A. Frisk, D. M. Burn, D. G. Newman, C. Klewe, A. T. N'Diaye, P. Shafer, E. Arenholz, G. J. Bowden, T. Hesjedal, G. van der Laan, G. Hrkac, and R. J. Hicken, Optically and microwave-induced magnetization precession in [Co/Pt]/NiFe exchange springs, ACS Appl. Mater. Interfaces **12**, 52116 (2020).

[3] J. E. Davies, O. Hellwig, E. E. Fullerton, J. S. Jiang, S. D. Bader, G. T. Zimányi, and K. Liu, Anisotropy dependence of irreversible switching in Fe/SmCo and FeNi/FePt exchange spring magnet films, Appl. Phys. Lett. **86**, 262503 (2005).

[4] E. E. Fullerton, J. S. Jiang, M. Grimsditch, C. H. Sowers, and S. D. Bader, Exchange-spring behavior in epitaxial hard/soft magnetic bilayers, Phys. Rev. B **58**, 12193 (1998).

[5] E. E. Fullerton, J. Jiang, and S. Bader, Hard/soft magnetic heterostructures: Model exchange-spring magnets, J. Magn. Magn. Mater. **200**, 392 (1999).

[6] J. S. Jiang and S. D. Bader, Rational design of the exchange-spring permanent magnet, J. Phys.: Condens. Matter **26**, 064214 (2014).

[7] C. Banerjee, S. Pal, M. Ahlberg, T. N. A. Nguyen, J. Åkerman, and A. Barman, All-optical study of tunable ultrafast spin dynamics in [Co/Pd]/NiFe systems: The role of spin-twist structure on Gilbert damping, RSC Adv. **6**, 80168 (2016).

[8] T. N. Anh Nguyen, R. Knut, V. Fallahi, S. Chung, Q. T. Le, S. M. Mohseni, O. Karis, S. Peredkov, R. K. Dumas, C. W. Miller, and J. Åkerman, Depth-Dependent Magnetization Profiles of Hybrid Exchange Springs, Phys. Rev. Appl. **2**, 044014 (2014).

[9] S. Jiang, S. Chung, Q. T. Le, P. K. J. Wong, W. Zhang, and J. Åkerman, Field-free high-frequency exchange-spring spin-torque nano-oscillators, Nano Lett. **23**, 1159 (2023).

[10] H. Zeng, J. Li, J. P. Liu, Z. L. Wang, and S. Sun, Exchange-coupled nanocomposite magnets by nanoparticle self-assembly, Nature (London) **420**, 395 (2002).

[11] G. B. G. Stenning, G. J. Bowden, S. A. Gregory, J.-M. L. Beaujour, P. A. J. de Groot, G. van der Laan, L. R. Shelford, P. Bencok, P. Steadman, A. N. Dobrynin, and T. Hesjedal, Magnetic reversal in a YFe_2 dominated $DyFe_2/YFe_2$ multilayer film, Appl. Phys. Lett. **101**, 072412 (2012).

[12] G. B. G. Stenning, G. J. Bowden, S. A. Gregory, P. A. J. de Groot, G. van der Laan, L. R. Shelford, P. Bencok, P. Steadman, A. N. Dobrynin, and T. Hesjedal, Transverse magnetic exchange springs in a $DyFe_2/YFe_2$ superlattice, Phys. Rev. B **86**, 174420 (2012).

[13] F. Magnus, M. E. Brooks-Bartlett, R. Moubah, R. A. Procter, G. Andersson, T. P. A. Hase, S. T. Banks, and B. Hjörvarsson, Long-range magnetic interactions and proximity effects in an amorphous exchange-spring magnet, Nat. Commun. **7**, ncomms11931 (2016).

[14] K. A. Thórarinsdóttir, T. Hase, B. Hjörvarsson, and F. Magnus, Amorphous exchange-spring magnets with crossed perpendicular and in-plane anisotropies, Phys. Rev. B **103**, 014440 (2021).

[15] Y. Liu, Y. Q. Wu, M. J. Kramer, Y. Choi, J. S. Jiang, Z. L. Wang, and J. P. Liu, Microstructure analysis of a SmCo/Fe exchange spring bilayer, Appl. Phys. Lett. **93**, 192502 (2008).

[16] H. D. Chopra, M. R. Sullivan, A. Ludwig, and E. Quandt, Magnetoelastic and magnetostatic interactions in exchange-spring multilayers, Phys. Rev. B **72**, 054415 (2005).

[17] K. Son and G. Schütz, Fabrication and temperature-dependent magnetic properties of large area $L1_0$-FePt/Co exchange-spring magnet nanopatterns, Phys. E **115**, 113687 (2020).

[18] T. N. A. Nguyen, Y. Fang, V. Fallahi, N. Benatmane, S. M. Mohseni, R. K. Dumas, and J. Åkerman, [Co/Pd]NiFe exchange springs with tunable magnetization tilt angle, Appl. Phys. Lett. **98**, 172502 (2011).

[19] D. J. Carnevale, M. Shatruk, and G. F. Strouse, Ligand passivated core-shell FePt@Co nanomagnets exhibiting enhanced energy product, Chem. Mater. **28**, 5480 (2016).

[20] F. Magnus, U. B. Arnalds, H. Palonen, G. K. Pálsson, H. Ali, K. Leifer, and B. Hjörvarsson, Tuneable exchange-spring stiffness in amorphous magnetic trilayer structures, J. Phys.: Condens. Matter **33**, 445803 (2021).

[21] F. Magnus, R. Moubah, A. H. Roos, A. Kruk, V. Kapaklis, T. Hase, B. Hjörvarsson, and G. Andersson, Tunable giant magnetic anisotropy in amorphous SmCo thin films, Appl. Phys. Lett. **102**, 162402 (2013).

[22] G. B. G. Stenning, A. R. Buckingham, G. J. Bowden, R. C. C. Ward, G. van der Laan, L. R. Shelford, F. Maccherozzi, S. S. Dhesi, and P. A. J. de Groot, Exchange-spring-driven spin flop in an $ErFe_2/YFe_2$ multilayer studied by x-ray magnetic circular dichroism, Phys. Rev. B **84**, 104428 (2011).

[23] J. P. Liu, C. P. Luo, Y. Liu, and D. J. Sellmyer, High energy products in rapidly annealed nanoscale Fe/Pt multilayers, Appl. Phys. Lett. **72**, 483 (1998).

[24] R. Pellicelli, C. Pernechele, M. Solzi, M. Ghidini, F. Casoli, and F. Albertini, Modeling and characterization of irreversible switching and viscosity phenomena in perpendicular exchange-spring Fe-FePt bilayers, Phys. Rev. B **78**, 184434 (2008).

[25] S. Tacchi, T. N. Anh Nguyen, G. Carlotti, G. Gubbiotti, M. Madami, R. K. Dumas, J. W. Lau, J. Åkerman, A. Rettori, and M. G. Pini, Spin wave excitations in exchange-coupled [Co/Pd]-NiFe films with tunable tilting of the magnetization, Phys. Rev. B **87**, 144426 (2013).

[26] S. Tacchi, T. N. A. Nguyen, G. Gubbiotti, M. Madami, G. Carlotti, M. G. Pini, A. Rettori, V. Fallahi, R. K. Dumas, and J. Åkerman, [Co/Pd]-CoFeB exchange spring magnets with tunable gap of spin wave excitations, J. Phys. D **47**, 495004 (2014).

[27] A. Haldar, C. Banerjee, P. Laha, and A. Barman, Brillouin light scattering study of spin waves in NiFe/Co exchange spring bilayer films, J. Appl. Phys. **115**, 133901 (2014).

[28] G. Carlotti and G. Gubbiotti, Magnetic properties of layered nanostructures studied by means of Brillouin light scattering and the surface magneto-optical Kerr effect, J. Phys.: Condens. Matter **14**, 8199 (2002).

[29] G. Gubbiotti, A. Sadovnikov, E. Beginin, S. Sheshukova, S. Nikitov, G. Talmelli, I. Asselberghs, I. P. Radu, C. Adelmann, and F. Ciubotaru, Magnonic band structure in CoFeB/Ta/NiFe meander-shaped magnetic bilayers, Appl. Phys. Lett. **118**, 162405 (2021).

[30] S. Roy, A. Connell, M. Ludwig, N. Wang, T. O'Donnell, M. Brunet, P. McCloskey, C. ÓMathúna, A. Barman, and R. Hicken, Pulse reverse plating for integrated magnetics on Si, J. Magn. Magn. Mater. **290-291**, 1524 (2005).

[31] N. Wang, T. O'Donnell, S. Roy, M. Brunet, P. McCloskey, and S. O'Mathuna, High-frequency micro-machined power inductors, J. Magn. Magn. Mater. **290-291**, 1347 (2005).

[32] J. Riveiro and M. Sanchez-Trujillo, Magnetic anisotropy of electrodeposited Co-P amorphous alloys, IEEE Trans. Magn. **16**, 1426 (1980).

[33] J. Riveiro and G. Rivero, Multilayered magnetic amorphous Co-P films, IEEE Trans. Magn. **17**, 3082 (1981).

[34] J. Riveiro, Annealing effects in electrodeposited amorphous Co-P alloys, J. Magn. Magn. Mater. **27**, 119 (1982).

[35] L. Perez, O. de Abril, M. Sanchez, C. Aroca, E. Lopez, and P. Sanchez, Electrodeposited amorphous CoP multilayers with high permeability, J. Magn. Magn. Mater. **215-216**, 337 (2000).

[36] I. Lucas, L. Perez, C. Aroca, P. Sanchez, E. Lopez, and M. Sanchez, Magnetic properties of CoP alloys electrodeposited at room temperature, J. Magn. Magn. Mater. **290-291**, 1513 (2005).

[37] P. McCloskey, B. Jamieson, T. O'Donnell, D. Gardner, M. A. Morris, and S. Roy, High-frequency nanostructured magnetic materials for integrated inductors, J. Magn. Magn. Mater. **320**, 2509 (2008).

[38] P. McCloskey, B. Jamieson, T. O'Donnell, D. Gardner, M. A. Morris, and S. Roy, Electrodeposited amorphous CoâP based alloy with improved thermal stability, J. Magn. Magn. Mater. **322**, 1536 (2010).

[39] P. McCloskey, T. O'Donnell, B. Jamieson, D. Gardner, M. A. Morris, and S. Roy, Electrochemical Fabrication of Multi-Nanolayers, in *Handbook of Nanoelectrochemistry: Electrochemical Synthesis Methods, Properties and Characterization Techniques* (Springer International Publishing, Cham, Germany, 2016), pp. 1–27.

[40] M. S. Safavi and F. C. Walsh, Electrodeposited Co-P alloy and composite coatings: A review of progress towards replacement

of conventional hard chromium deposits, Surf. Coat. Technol. **422**, 127564 (2021).

[41] D. A. Gilbert, G. T. Zimanyi, R. K. Dumas, M. Winklhofer, A. Gomez, N. Eibagi, J. L. Vicent, and K. Liu, Quantitative decoding of interactions in tunable nanomagnet arrays using first order reversal curves, Sci. Rep. **4**, 4204 (2014).

[42] D. A. Gilbert, P. D. Murray, J. De Rojas, R. K. Dumas, J. E. Davies, and K. Liu, Reconstructing phase-resolved hysteresis loops from first-order reversal curves, Sci. Rep. **11**, 4018 (2021).

[43] R. Egli, VARIFORC: An optimized protocol for calculating non-regular first-order reversal curve (FORC) diagrams, Glob. Planet. Change **110**, 302 (2013), magnetic iron minerals in sediments and their relation to geologic processes, climate, and the geomagnetic field.

[44] R. J. Harrison and J. M. Feinberg, FORCinel: An improved algorithm for calculating first-order reversal curve distributions using locally weighted regression smoothing, Geochemistry, Geophysics, Geosystems **9**, (2008).

[45] S. Kulkarni and S. Roy, Deposition of thick Co-rich CoPtP films with high energy product for magnetic microelectromechanical applications, J. Magn. Magn. Mater. **322**, 1592 (2010).

[46] D. Mallick, K. Paul, T. Maity, and S. Roy, Magnetic performances and switching behavior of Co-rich CoPtP micromagnets for applications in magnetic MEMS, J. Appl. Phys. **125**, 023902 (2019).

[47] J. F. Callejas, C. G. Read, E. J. Popczun, J. M. McEnaney, and R. E. Schaak, Nanostructured Co_2P electrocatalyst for the hydrogen evolution reaction and direct comparison with morphologically equivalent CoP, Chem. Mater. **27**, 3769 (2015).

[48] A. Hubert and R. Schäfer, *Magnetic Domains: The Analysis of Magnetic Microstructures* (Springer Science & Business Media, New York, 2008), Chaps. 3 and 5.

[49] H. Takahashi, S. Tsunashima, S. Iwata, and S. Uchiyama, Measurement of magnetostriction constants in (111)-oriented polycrystalline PdCo alloy and multilayered films, Jpn. J. Appl. Phys. **32**, L1328 (1993).

[50] G. Ausanio, V. Iannotti, L. Lanotte, M. Carbucicchio, and M. Rateo, Weak stripe domains in Co/Fe multilayers, J. Magn. Magn. Mater. **226-230**, 1740 (2001).

[51] D. Ciudad, J. L. Prieto, I. Lucas, C. Aroca, and P. Sánchez, Optimization of magnetic properties of electrodeposited CoP multilayers for sensor applications, J. Appl. Phys. **101**, 043907 (2007).

[52] Y. Sun, W. Li, P. Dhagat, and C. R. Sullivan, Perpendicular anisotropy in granular CoZrO films, J. Appl. Phys. **97**, 10N301 (2005).

[53] S. Choudhury, A. K. Chaurasiya, A. K. Mondal, B. Rana, K. Miura, H. Takahashi, Y. Otani, and A. Barman, Voltage controlled on-demand magnonic nanochannels, Sci. Adv. **6**, eaba5457 (2020).

[54] S. Tacchi, G. Gubbiotti, M. Madami, and G. Carlotti, Brillouin light scattering studies of 2D magnonic crystals, J. Phys.: Condens. Matter **29**, 073001 (2017).

[55] A. F. Franco, C. Gonzalez-Fuentes, J. Åkerman, and C. Garcia, Anisotropy constant and exchange coupling strength of perpendicularly magnetized CoFeB/Pd multilayers and exchange springs, Phys. Rev. B **95**, 144417 (2017).

[56] S. N. Panda, S. Mondal, J. Sinha, S. Choudhury, and A. Barman, All-optical detection of interfacial spin transparency from spin pumping in β-Ta/CoFeB thin films, Sci. Adv. **5**, eaav7200 (2019).

[57] L. R. Shelford, Y. Liu, U. Al-Jarah, P. A. J. de Groot, G. J. Bowden, R. C. C. Ward, and R. J. Hicken, Ultrafast Optical Parametric Pumping of Magnetization Reorientation and Precessional Dynamics in $DyFe_2/YFe_2$ Exchange Springs, Phys. Rev. Lett. **113**, 067601 (2014).

[58] P. Grünberg, Light scattering from spin waves in thin films and layered magnetic structures, in *Light Scattering in Solids V: Superlattices and Other Microstructures*, edited by M. Cardona and G. Güntherodt (Springer, Berlin, 1989), pp. 303–335.

[59] J. Sinha, C. Banerjee, A. K. Chaurasiya, M. Hayashi, and A. Barman, Improved magnetic damping in CoFeB|MgO with an N-doped Ta underlayer investigated using the Brillouin light scattering technique, RSC Adv. **5**, 57815 (2015).

[60] W. F. Oliver, C. A. Herbst, S. M. Lindsay, and G. H. Wolf, A general method for determination of Brillouin linewidths by correction for instrumental effects and aperture broadening: Application to high-pressure diamond anvil cell experiments, Rev. Sci. Instrum. **63**, 1884 (1992).

[61] J. R. Sandercock and W. Wettling, Light scattering from surface and bulk thermal magnons in iron and nickel, J. Appl. Phys. **50**, 7784 (1979).

[62] G. Gubbiotti, G. Carlotti, J. Weston, G. Zangari, D. Crew, and R. Stamps, Asymmetry in the static and dynamic magnetic properties of a weak exchange spring trilayer, J. Magn. Magn. Mater. **286**, 479 (2005).

[63] R. Hicken, D. Eley, M. Gester, S. Gray, C. Daboo, A. Ives, and J. Bland, Brillouin light scattering studies of magnetic anisotropy in epitaxial Fe/GaAs films, J. Magn. Magn. Mater. **145**, 278 (1995).

[64] M. G. Cottam, Lineshape calculations for light scattering from spin-waves in absorptive magnetic materials, J. Phys. C **11**, 165 (1978).

[65] S. M. Rezende, A. Azevedo, M. A. Lucena, and F. M. de Aguiar, Anomalous spin-wave damping in exchange-biased films, Phys. Rev. B **63**, 214418 (2001).

[66] See Supplemental Material at http://link.aps.org/supplemental/10.1103/PhysRevB.107.214449 for a detailed analytical formulation of the evolution of the ES state from the non-ES state. It also describes the equation which has been used for asymmetric fittings of the bulk peaks.